Available online at www.sciencedirect.com
ScienceDirect
Trans. Nonferrous Met. Soc. China 33(2023) 1729−1741
Transactions of Nonferrous Metals Society of China
www.tnmsc.cn

Microstructural evolution and mechanical properties of cooling medium assistant friction stir processed AZ31B Mg alloy

Nan XU[1], Zi-ke REN[1], Yue FAN[1], Bo-kun GU[1], Jun SHEN[2,3], Qi-ning SONG[1], Jian-hua ZHAO[1], Ye-feng BAO[1]

1. College of Mechanical and Electrical Engineering, Hohai University, Changzhou 213022, China;
2. National Engineering Research Center for Magnesium Alloys, Chongqing University, Chongqing 400044, China;
3. College of Material Science and Engineering, Chongqing University, Chongqing 400044, China

Received 13 January 2022; accepted 20 April 2022

Abstract: AZ31B magnesium alloy prepared by conventional friction stir processing (FSP) usually exhibits an intense basal texture, resulting in an unsatisfactory strength and ductility. In this work, cooling medium-assisted FSP was conducted on the AZ31B magnesium alloy. The effects of a liquid CO_2 coolant on the thermal cycle, microstructure, and mechanical properties of the stir zone (SZ) were evaluated. The adoption of a liquid CO_2 coolant resulted in markedly decreased peak temperature and increased cooling rate. The SZ exhibited a fine grain structure with abundant dislocations and $\{10\bar{1}2\}$ twins. The grain refinement mechanism was attributed to the combinational effect of discontinuous dynamic recrystallization, continuous dynamic recrystallization, and twinning-induced geometric dynamic recrystallization. The SZ showed a best combination of ultimate tensile strength of 293 MPa and fracture elongation of 18.6%. The interaction of dislocations and $\{10\bar{1}2\}$ twins rendered the plastic deformation more stable during tensile testing.

Key words: Mg alloy; friction stir processing; Zenner−Hollomon parameter; recrystallization; microstructural evolution; mechanical properties

1 Introduction

Owing to their low density and high specific strength, magnesium (Mg) alloys are frequently used in aerospace, rail transportation, automotive industry, and manufacture of 3C (computer, communication, and consumer electronic) products [1,2]. However, Mg alloys possess a hexagonal close-packed crystalline structure and thus have limited slip systems, which endow them poor plastic deformability at room temperature [3,4]. Therefore, Mg alloys are usually prepared by die casting, hot extrusion, or hot rolling. Compared with cast Mg alloys, wrought Mg alloys exhibit relatively satisfactory strength–ductility synergy because dynamic recrystallization (DRX) promotes the formation of a fine grain structure [5]. Grain refinement enhances the strength and ductility of metals and alloys. Severe plastic deformation (SPD) is an effective technique to prepare ultrafine and even nanograined materials [6]. However, massive dislocations are introduced in the grain interior, resulting in the reduced ductility. Subsequent annealing can enhance the ductility of SPD materials by decreasing the dislocation density without substantial grain coarsening [7].

Friction stir processing (FSP) is a recently developed microstructure modification method based on friction stir welding (FSW) technology [8]. During FSP, the materials undergo the plastic deformation and high-temperature treatment, similar to SPD and subsequent annealing. Fine or ultrafine grain structure with few dislocations is produced in the stir zone (SZ). Good strength–ductility synergy of the FSP Mg alloys is achieved,

Corresponding author: Nan XU, Tel: +86-519-85192039, E-mail: xunan@hhu.edu.cn
DOI: 10.1016/S1003-6326(23)66217-X

which is attributed to remarkable grain refinement. However, an intense basal texture is generated in the SZ, which markedly degrades the mechanical properties of FSP Mg alloys [9]. $\{10\bar{1}2\}$ twins can randomize the basal texture of Mg alloys, but the $\{10\bar{1}2\}$ twinning behavior is sensitive to the processing temperature [10]. The processing temperature of traditional FSP is relatively high, hindering the generation of $\{10\bar{1}2\}$ twins during FSP. XIN et al [11] conducted cold rolling on the FSW-treated AZ31 Mg alloy. The strength and ductility were enhanced owing to basal texture randomization caused by the activity of the $\{10\bar{1}2\}$ twinning behavior. However, this technology is relatively complicated in practice. In previous studies on FSW of Cu alloys, XU et al [12,13] found that adopting an additional cooling medium can enhance the cooling rate and reduce the processing temperature; thus, the substructures generated during deformation were retained in the SZ to enhance the strength and ductility of the welded joint. Furthermore, the combinative effect of deformation temperature and strain rate on grain size is usually determined by Zenner−Hollomon (Z) parameter. During the FSP, the Z parameter can be changed by adjusting the tool rotating rate and processing speed. The relationship among the microstructure, mechanical properties, and Z parameter of FSP Mg alloys is still unclear. In addition, the cooling rate also plays an important role in the final grain structure by affecting the grain growth just after the FSP. If the cooling rate is enhanced, grain coarsening will be significantly limited, and it is convenient to understand how the Z parameter affects the actual microstructural evolution and mechanical properties of the SZ. In the current study, cooling medium-assisted FSP (CMA-FSP) was further applied on the AZ31B Mg alloy. Fine grains with massive dislocations and $\{10\bar{1}2\}$ twins were directly produced in the SZ. The microstructure evolution and mechanical properties of conventional and CMA-FSP AZ31B Mg alloys were investigated, and the relationship among Z parameter, microstructure, and mechanical properties was also discussed.

2 Experimental

Commercially wrought AZ31B Mg alloy plates with dimensions of 200 mm × 100 mm × 3 mm were selected as research targets in this study. A location-control mode FSW machine (FSW-LM-BM16, CFSW, China) was used in this study. The dimensions of the tool and the processing parameters are summarized in Tables 1 and 2, respectively. A schematic of the CMA-FSP is presented in Fig. 1. The liquid CO_2 nozzle was placed behind the rotating tool with a movement speed the same as the processing speed. A K-type thermocouple was placed under the Mg alloy sheet and set in the groove of the back plate to record the temperature history of the SZ. After processing, the cross-sections for microstructural characterization were cut perpendicularly to the processing direction (PD). Electron backscatter diffraction (EBSD, EDAX TSL OIM™, USA) measurement was conducted to investigate the microstructural evolution of the materials. The EBSD device was set in a scanning electron microscope (SEM, JSM−7500, JEOL Ltd., Japan), and the step size was 0.4 μm. The EBSD specimens were prepared by electrochemical

Table 1 Dimensions of tool (WC−Co based steel)

Shoulder diameter/mm	Probe diameter/mm	Probe length/mm
15	6	2.8

Table 2 Friction stir processing parameters

Label	Rotation rate/ (r·min^{-1})	Cooling medium	Processing speed/ (mm·min^{-1})	Load/ kN	Tilt angle/ (°)
R600-A*	600	Air	200	9.8	2.5
R800-A	800	Air			
R1000-A	1000	Air			
R1000-LC**	1000	Liquid-CO_2			

* A means air cooling, ** LC means liquid CO_2 cooling

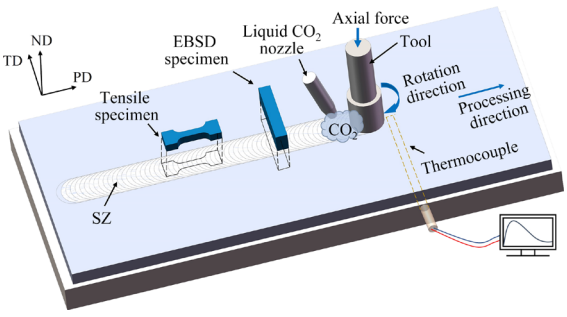

Fig. 1 Schematic diagram of CMA-FSP (The processing direction, transverse direction, and plate normal direction are indicated by PD, TD, and ND, respectively)

polishing using a commercial AC2 electrolyte at −30 °C and 25 V. In accordance with the GB/T 228.1—2010 standard, three tensile specimens with gauge dimensions of 12 mm × 4 mm × 1.8 mm were cut parallel to the PD. Tensile tests were conducted using an electronic universal testing machine with a strain rate of 1×10^{-3} s^{-1}. To investigate the effect of $\{10\bar{1}2\}$ twins on the mechanical properties of AZ31B magnesium alloy, the tensioned CMA-FSP sample was further characterized by a transmission electron microscope (TEM, JEM−2100, JEOL, Ltd., Japan). The TEM specimen was initially mechanically polished to 50 μm and then double-jet electropolished using AC2 electrolyte at −30 °C and 20 V.

3 Results and discussion

3.1 Temperature history

The temperature histories of the SZs are presented in Fig. 2. The three SZs obtained by traditional FSP exhibited similar temperature histories. When the rotating tool approached the thermocouple, the temperature increased sharply. When the tool passed through and left the thermocouple, the temperature decreased slowly. The peak temperatures of R1000-A, R800-A, and R600-A were 462, 433, and 402 °C, respectively, indicating that decreasing the rotation rate can reduce the peak temperature in the SZ. However, the SZs in traditional FSP showed a similar cooling rate of 16 °C/s from the peak temperature to room temperature. The workpiece and tool in CMA-FSP were drastically cooled by the adoption of a liquid CO_2 coolant; thus, the SZ of R1000-LC exhibited a reduced processing temperature of 355 °C, and the cooling rate increased to 47 °C/s. The high-temperature durations above 100 °C were 13.5, 9.7, 8.2, and 4.3 s for R1000-A, R800-A, R600-A, and R1000-LC, respectively. Evidently, the post-annealing effect was successfully eliminated by the adoption of a liquid CO_2 coolant.

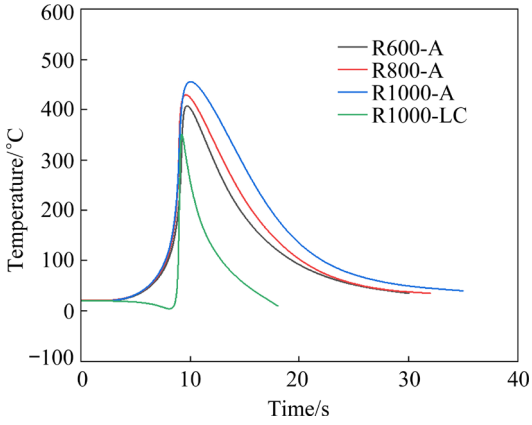

Fig. 2 Temperature histories of SZs obtained by friction stir processing under different conditions

3.2 Microstructural evolution

Figure 3 shows the EBSD results of the as-received AZ31B Mg alloy. The white and black lines in the inverse pole figure indicate a low-angle grain boundary (LAGB, $2°\leq\theta<15°$) and a high-angle grain boundary (HAGB, $\theta\geq15°$), respectively. The as-received material exhibits equiaxed grains with an average grain size of 13 μm, and the HAGB rate is 84%. The (0001) pole figure indicates that the *c*-axis of most grains is almost parallel to the normal direction (ND). Such a texture is frequently observed in hot-rolled Mg alloys [14].

Figure 4 shows the inverse pole figures of SZs obtained by FSP under different conditions. All SZs

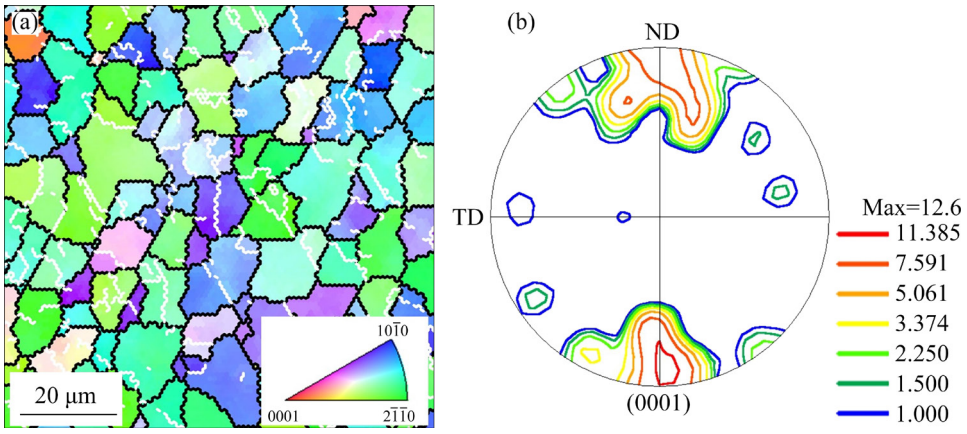

Fig. 3 EBSD results of base metal (BM): (a) Inverse pole figure; (b) (0001) pole figure

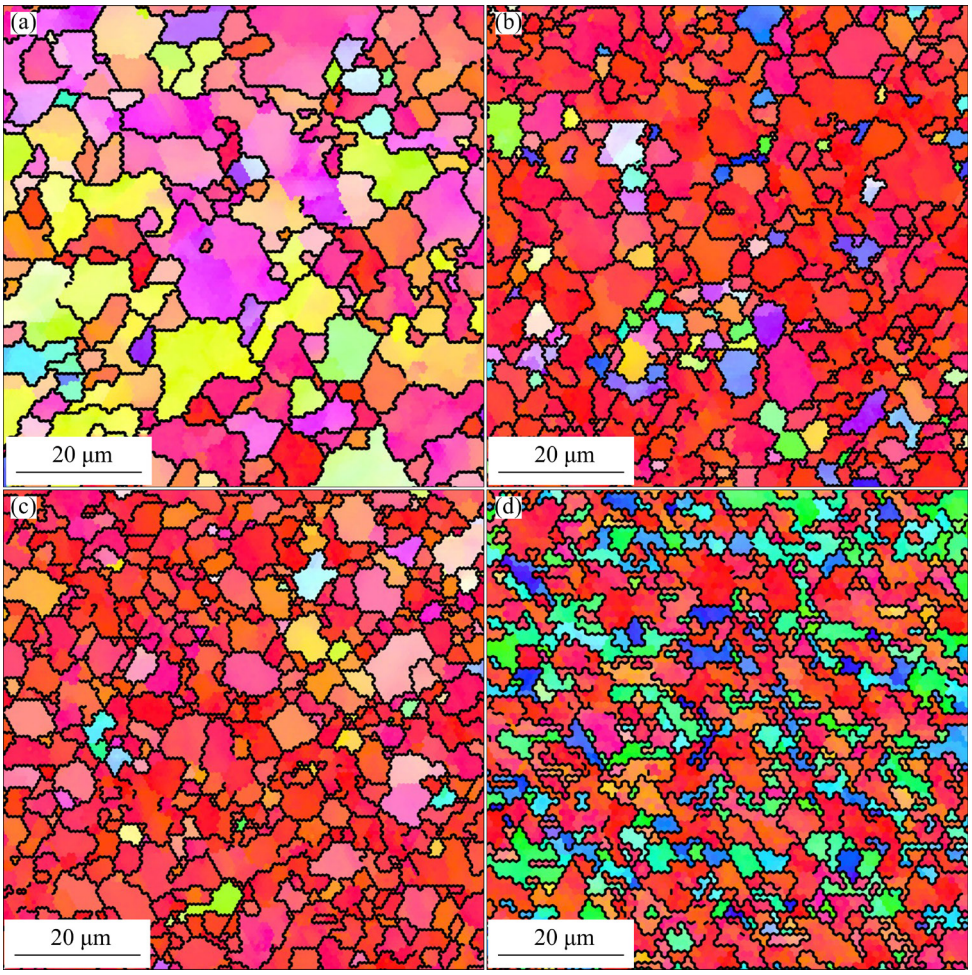

Fig. 4 Inverse pole figures of SZs obtained by FSP under different conditions: (a) R1000-A; (b) R800-A; (c) R600-A; (d) R1000-LC

exhibit a refined grain structure relative to that of the as-received material shown in Fig. 3(a). Without liquid CO_2 cooling, the grain size is slightly refined from 8.2 to 5.5 μm by decreasing the rotation rate from 1000 to 600 r/min. This result demonstrates that the grain structure of the FSP-treated Mg alloy can be refined by reducing the heat input [15]. With the adoption of a liquid CO_2 coolant, the grain size is significantly reduced to 2.2 μm. Figures 5 and 6 present the grain boundary maps and the misorientation angle distribution of the SZs, respectively. In traditional FSP, the LAGB rate decreased with an increase in the rotation rate. Although the heat input was reduced, no significant changes in misorientation distributions were observed. By contrast, the misorientation distribution of R1000-LC had two peaks: one located at θ=2°−15°, indicating that the LAGB rate significantly increased to 36.4%, and the other located at θ=86.3°, which was mainly attributed to the $\{10\bar{1}2\}$ twin boundaries [16]. Figure 7 shows the Kernel average misorientation (KAM) maps, which describes the misorientation angles lower than 5° in the SZs. The KAM value corresponds to the dislocation density in the SZ [17]. The SZ of R1000-LC showed a larger KAM value than the SZs obtained by traditional FSP. Owing to the reduced processing temperature and increased cooling rate, the post-annealing effect was eliminated. The annihilation and rearrangement of dislocations were impeded, allowing the retention of a large number of dislocations in the SZ. Therefore, massive substructures, including the dislocations and $\{10\bar{1}2\}$ twins, were successfully introduced into the fine grains because of the adoption of a liquid CO_2 coolant.

The grain size of the FSP-treated Mg alloy was determined by the synergic influence of the strain rate ($\dot{\varepsilon}$) and the processing thermodynamic temperature (T). The synergistic effect of processing

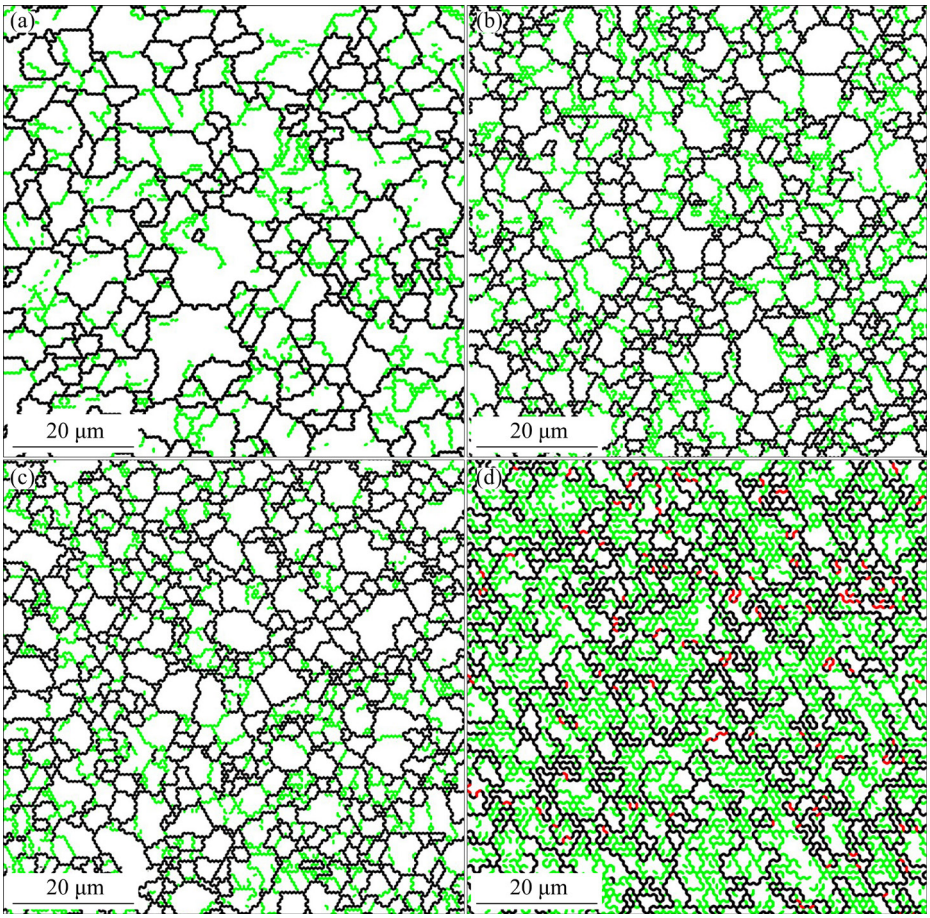

Fig. 5 Grain boundary maps of SZs obtained by FSP under different conditions: (a) R1000-A; (b) R800-A; (c) R600-A; (d) R1000-LC (The LAGB, HAGB, and the twin boundary (TB, θ=86.3°±5°) are represented by green, black, and red lines, respectively)

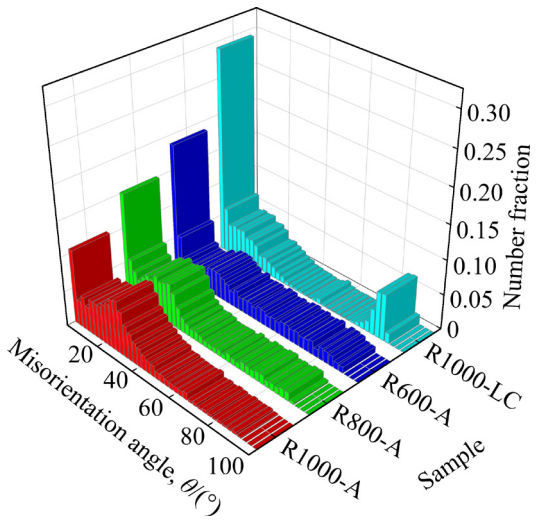

Fig. 6 Misorientation angle distribution of SZs obtained by FSP under different conditions

temperature and strain rate is described by the Zener–Hollomon (Z) parameter [18,19]:

$$Z = \dot{\varepsilon}\exp[Q/(RT)] \quad (1)$$

where Q (=135 kJ/mol) is the activation energy for deformation and R (=8.314 J/(mol·K)) is the molar gas constant. During FSP, the materials underwent high-temperature plastic deformation similar to that of high-pressure torsion at elevated temperatures. Compared with that around the high-speed rotating probe, the material flow rate around the probe was relatively low because of a rotating lag [20]. CHANG et al [19] developed a model to predict the strain rate during FSP:

$$\dot{\varepsilon} = 2\pi r_e R_m / L_e \quad (2)$$

where r_e and L_e are the radius and the depth of the SZ, respectively, and R_m is half of the tool rotation rate. The measured peak temperature and calculated strain rate of FSP under different conditions are summarized in Table 3. The strain rate increased with increasing rotation rate. The strain rate during the FSP was markedly higher than those obtained by traditional SPD technologies, such as equal-channel angular pressing [21,22], extrusion [23],

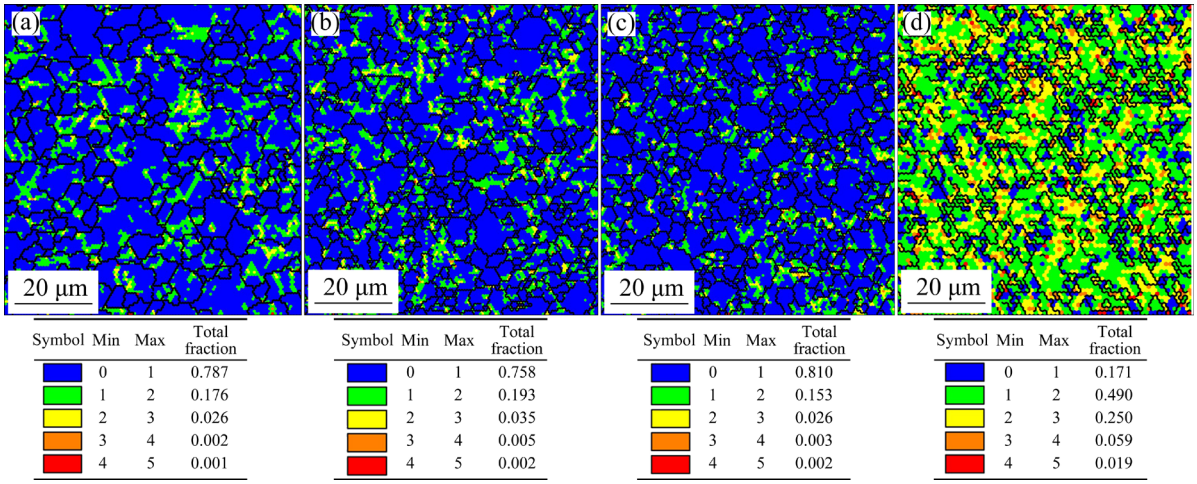

Fig. 7 Kernel average misorientation (KAM) maps of SZs obtained by FSP under different conditions: (a) R1000-A; (b) R800-A; (c) R600-A; (d) R1000-LC

Table 3 Calculated Z parameters under various FSP conditions

Sample	$\dot{\varepsilon}$ /s^{-1}	T/°C	ln(Z/s^{-1})
R1000-A	93.4	462	26.6
R800-A	74.8	437	27.2
R600-A	56.1	402	28.1
R1000-LC	78.5	355	30.3

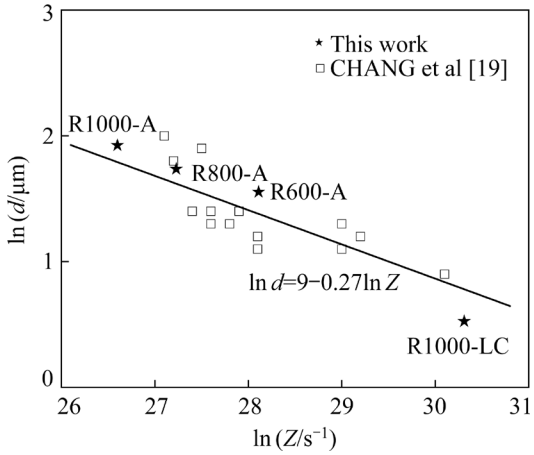

Fig. 8 Relationship between Z parameter and grain size

and rolling [24]. The Z parameters of FSP-treated AZ31 Mg alloy under different conditions can be calculated based on Eq. (1); the obtained results are listed in Table 3. Figure 8 depicts the relationship between the grain size of the FSP-treated AZ31 Mg alloy and the Z parameter. The range of Z parameters obtained in the current study was slightly enlarged relative to that of the model predicted by CHANG et al [19]. The Z parameters obtained by traditional FSP were well matched to those of the classic model, whereas the Z parameter of R1000-LC deviated from this line. It was attributed to the $\{10\bar{1}2\}$ twin boundaries that divided a recrystallized grain into several grains, inducing an apparent reduction in the grain size.

Figure 9 shows the (0001) and $(10\bar{1}1)$ pole figures of the SZs obtained by FSP under different conditions. Traditional FSP-treated AZ31 Mg alloys exhibited a basal texture of ⟨0001⟩//PD, and the texture intensity gradually increased because of an increase in the rotation rate. However, the AZ31 Mg alloy treated by CMA-FSP exhibited two textural components of ⟨0001⟩//ND and ⟨0001⟩//PD, and the textural intensity was markedly reduced. The Z parameters of traditional FSP-treated alloy were relatively low, rendering the basal slip the dominant deformation mechanism. The {0001} crystalline plane was parallel to the probe surface, resulting in the formation of the ⟨0001⟩//PD component [25]. Notably, both the ⟨0001⟩//ND and ⟨0001⟩//PD components were generated in CMA-FSP-treated alloy. As the Z parameter increased, the $\{10\bar{1}2\}$ twinning behavior was activated [26]. The texture components were determined by the processing temperature and the deformation mode. The $\{10\bar{1}2\}$ twinning behavior was activated via compression deformation perpendicular to the c-axis and the tensile deformation parallel to the c-axis [27]. During FSP, the shear force and axial force provided tensile stress and compressive stress (Fig. 10), respectively. To coordinate the plastic deformation along the c-axis, the $\{10\bar{1}2\}$ twinning behavior in the ⟨a+c⟩ direction was activated. Such

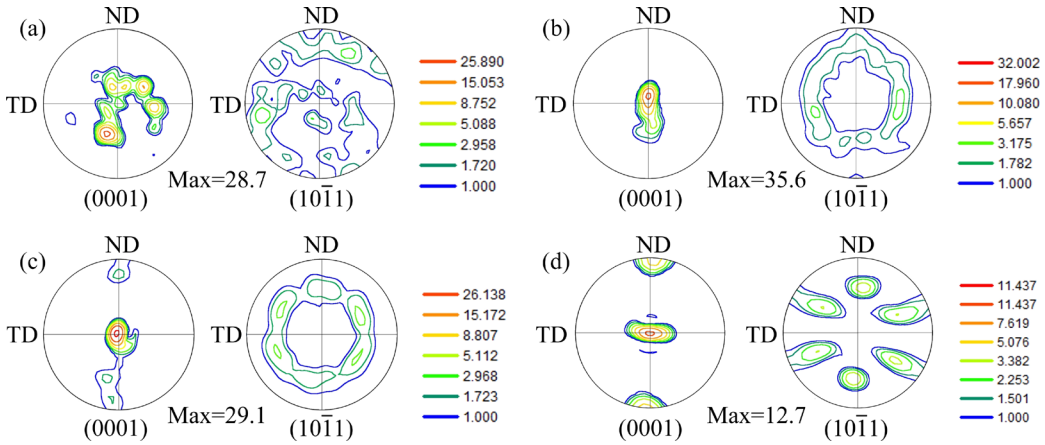

Fig. 9 (0001) and $(10\bar{1}1)$ pole figures of SZs obtained by FSP under different conditions: (a) R600-A; (b) R800-A; (c) R1000-A; (d) R1000-LC

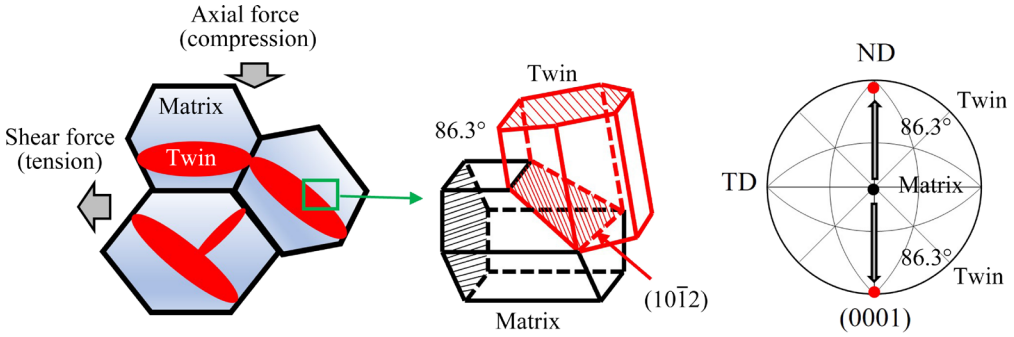

Fig. 10 Schematic diagrams of $\{10\bar{1}2\}$ twinning behavior

$\{10\bar{1}2\}$ twins rotated along the {0001} crystalline plane backward by about 86.3° toward the ND, leading to the formation of the ⟨0001⟩//ND component and the randomization of the basal texture.

A detailed investigation of the thermo-mechanically affected zone (TMAZ) can explain the microstructural evolution during FSP [28,29]. In the present study, the TMAZ of R1000-LC was characterized by EBSD because the liquid CO_2 coolant can eliminate dislocation recovery and grain coarsening. The results are shown in Figs. 11 and 12. On the basis of the EBSD results, grain refinement during FSP was attributed to the combinational effects, including discontinuous DRX, continuous DRX, and twinning-induced geometric DRX. In a previous study on a Mg alloy treated by FSP, grain refinement was usually attributed to discontinuous DRX and continuous DRX [30]. However, no research on twinning-induced geometric DRX has been reported. To elucidate the grain refinement mechanism of the Mg alloy subjected to FSP, several schematics for various DRX phenomena are shown in Fig. 13.

(1) Discontinuous DRX. Grain boundaries hindered the movement of dislocations, hence the relatively high dislocation density generated in the vicinity of the grain boundary. The difference in dislocation density at the grain boundary was the driving force for grain boundary migration, resulting in the "bulging" of grain boundaries (Region *A* in Fig. 11). To confirm this phenomenon, the KAM map of Region *A* is shown in Fig. 12(a). Different KAM values at the grain boundary represented the different dislocation densities. As deformation further continued, continuous dislocation accumulation caused the formation of dislocation cells, LAGBs and the generation of subgrains behind the bulged grain boundaries. Subsequently, the subgrain boundaries absorbed the dislocations and transformed them into HAGBs, ultimately producing new grains [31,32]. Fine discontinuous DRX grains frequently formed at the original grain boundaries, hence a typical necklace structure appeared in the TMAZ, as indicated by a black dotted oval in Fig. 11.

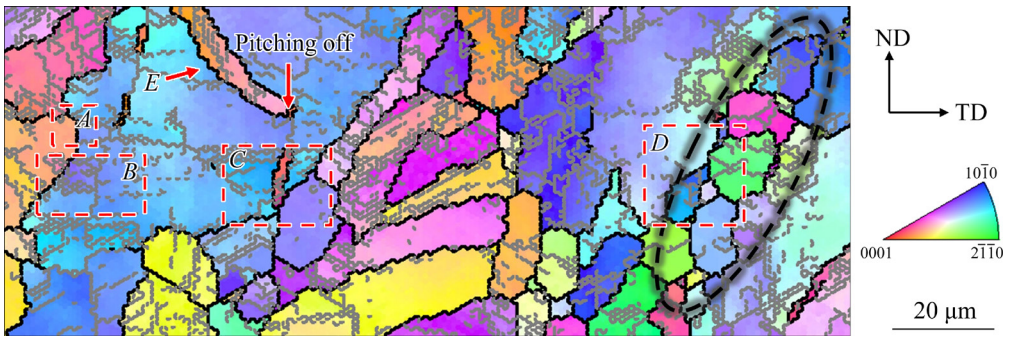

Fig. 11 Inverse pole figure of TMAZ in R1000-LC

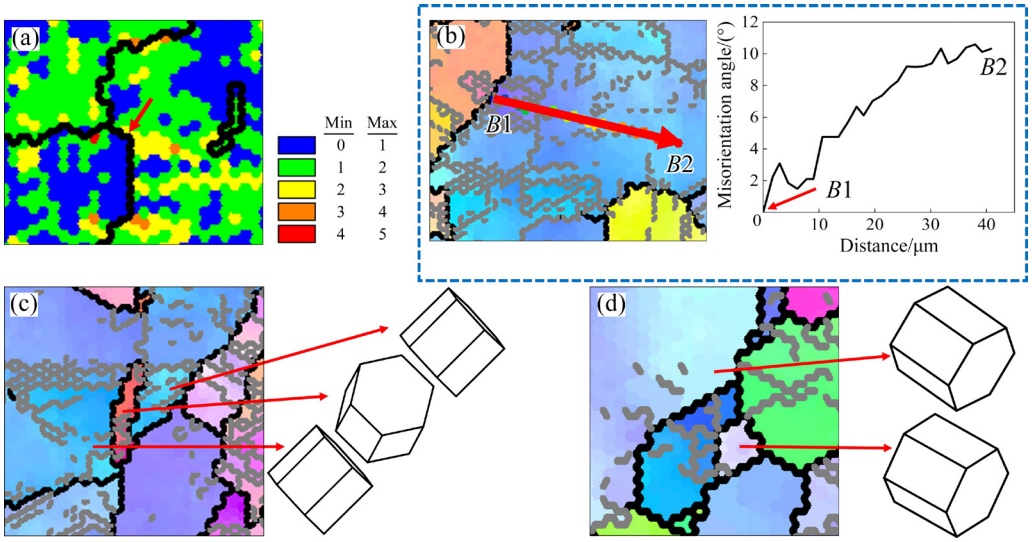

Fig. 12 Enlarged images of selected areas in Fig. 11: (a) KAM map of Region *A*; (b) Point-to-origin misorientation of Region *B*; (c, d) Three-dimensional crystalline models of Regions *C* and *D*, respectively

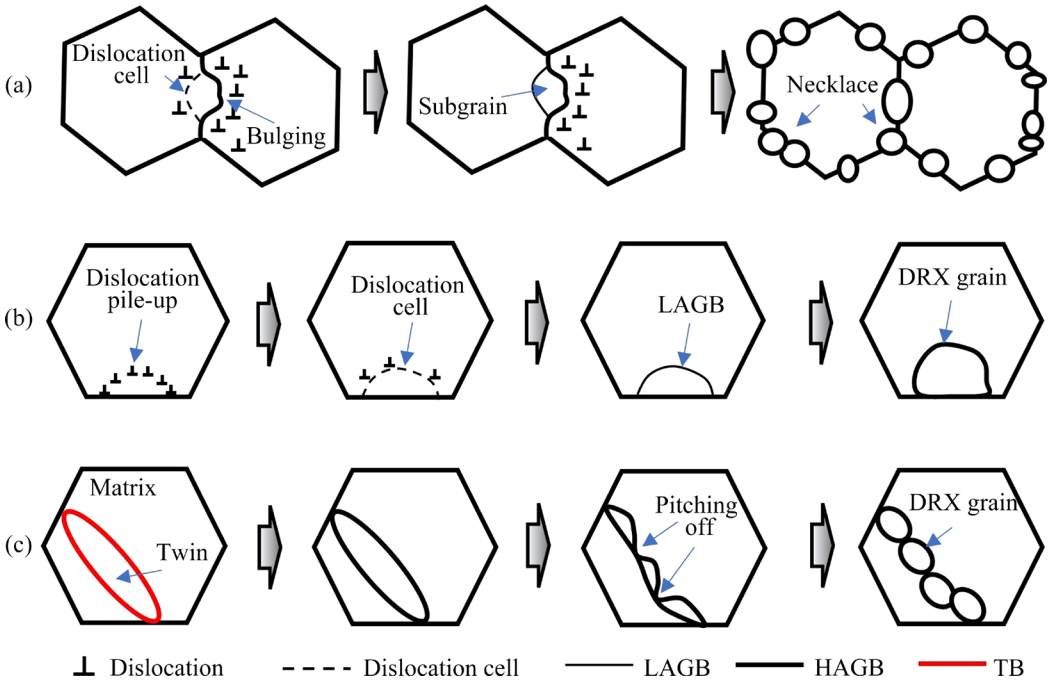

Fig. 13 Schematic diagrams of several dynamic recrystallization mechanisms during FSP of AZ31B magnesium alloy: (a) Discontinuous DRX; (b) Continuous DRX; (c) Twinning-induced geometric DRX

(2) Continuous DRX. Mg alloys have moderate stacking fault energy; thus, dynamic recovery frequently occurs to consume dislocations during high-temperature plastic deformation [33,34]. The dislocation density in the vicinity of the original grain boundaries may not be sufficiently large to induce "bulging" (Region *B* in Fig. 11). Instead, dislocation cells and LAGBs are formed locally via dynamic recovery. As shown in Fig. 12(b), the cumulative misorientation indicated a significant increase in misorientation from the grain boundary to the grain interior (along the red arrow from *B*1 to *B*2). LAGBs are then directly transformed into HAGBs by subgrain rotation, prompting the formation of new grains.

(3) Twinning-induced geometric DRX. A grain was accidentally formed in the grain interior (Region *C* in Fig. 11). The three-dimensional crystalline models indicated that this grain originated from the $\{10\bar{1}2\}$ twin (Fig. 12(c)). Initially, the shear force and axial force introduced from the rotating tool promoted the generation of the $\{10\bar{1}2\}$ twins. As deformation continuously proceeded, straight TBs changed into a serrated morphology, as indicated by Arrow *E* in Fig. 11. Meanwhile, part of the TBs lost the perfect twin/matrix relationship and then changed into HAGBs. Finally, "pitching off" occurred between the serrated TBs or HAGBs, forming new grains [30]. Furthermore, to confirm different DRX mechanisms for texture changing, the grain orientation of Region *D* is shown in Fig. 12(d). The orientation of continuous and discontinuous DRX grains (no substructure) was similar to that of the original grain, indicating that the continuous and discontinuous DRX mechanisms did not contribute to the texture change, i.e., the texture randomization was mainly attributed to the twinning-induced geometric DRX mechanism.

3.3 Mechanical properties

The stress–strain curves and mechanical properties of SZs generated during FSP under different conditions are presented in Fig. 14. In traditional FSP, with a decrease in the rotation rate, the ultimate tensile strength increased from 255 to 285 MPa owing to grain refinement. The elongation also increased from 16.7% to 19.8% because the basal texture intensity was reduced. In CMA-FSP, without changing the processing parameters, the ultimate tensile strength was significantly improved to 293 MPa, and the elongation was not markedly reduced, indicating that the uniform plastic deformation stage was more stable than that in traditional FSP.

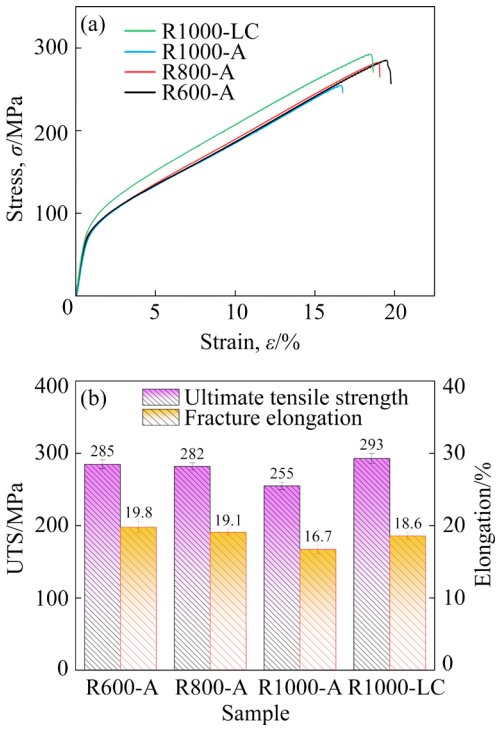

Fig. 14 Stress–strain curves (a) and mechanical properties (b) of SZs obtained by FSP under different conditions

During uniform plastic deformation, the flow stress is typically described by the Hollomon relationship [35]:

$$\lg(\sigma-\sigma_s)=K+n\lg(\varepsilon-\varepsilon_s) \quad (3)$$

where σ is the true stress, σ_s is the yield stress, n is the strain hardening index, and K is a constant. According to Eq. (3), the calculated n values in FSP under different conditions are shown in Fig. 15. The n value in CMA-FSP was lower than that in traditional FSP, indicating that the local stress concentration during plastic deformation was relieved. This occurrence was attributed to the interaction between the dislocations and the $\{10\bar{1}2\}$ twins [36].

The TEM results of tensioned R1000-LC sample are shown in Fig. 16. Based on the bright-field TEM image as shown in Fig. 16(a), several dislocations were detected near the TB. The high-resolution TEM image associated with the Fourier

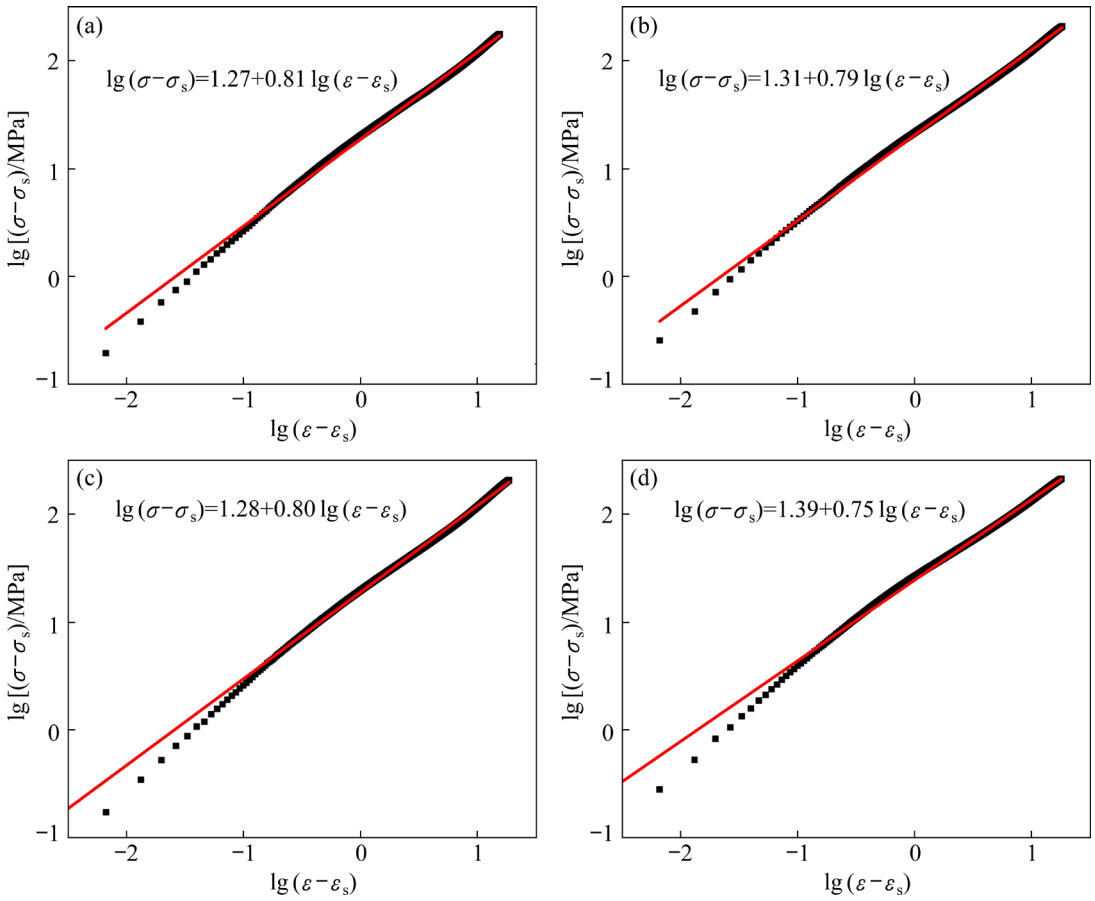

Fig. 15 Strain hardening index of SZ in FSP under different conditions: (a) R1000-A; (b) R800-A; (c) R600-A; (d) R1000-LC

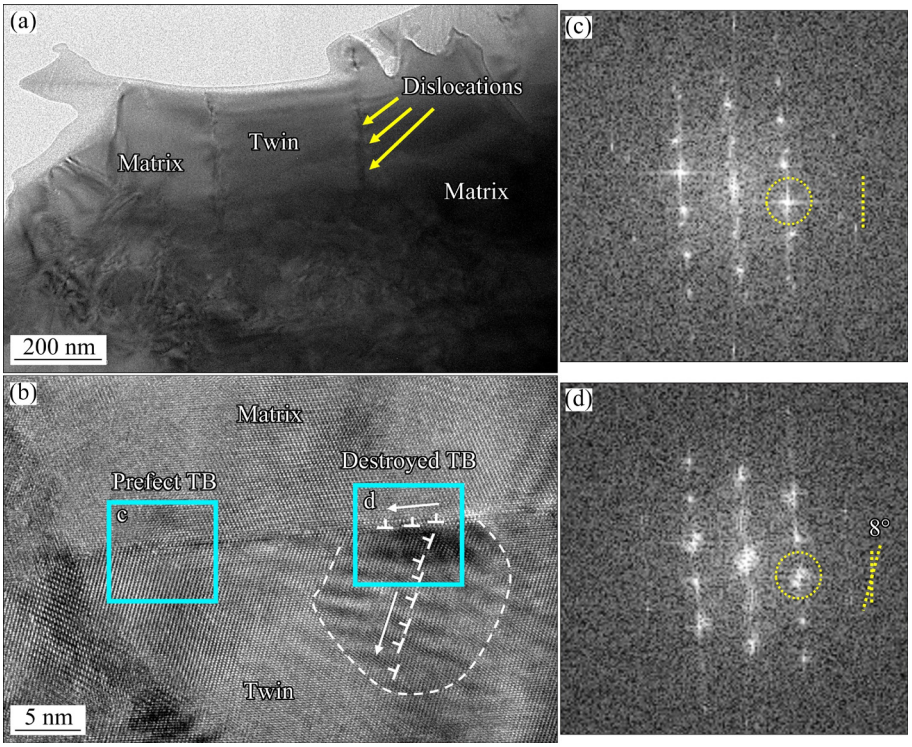

Fig. 16 TEM images of tensioned R1000-LC sample (a, b) and Fourier transform images of selected regions (c, d): (a) Low magnification; (b) High magnification

transform image indicated that some partial dislocations were distributed at the TB, resulting in the reciprocal point deviating from an exact twin/matrix relationship of 8° (Figs. 16(b−d)). XIN et al [37] investigated the TB migration of AZ31 magnesium alloy, and it was found that this deviation was attributed to the interaction of dislocation and TB. The TB can provide a certain space for the dislocation movement, thus no dislocation pile-up was found at the TB. In addition, during the tension, when the dislocation in the hexagonal close-packed lattice moved to the $\{10\bar{1}2\}$ TB, a partial dislocation was emitted into the twined region and a Shockley partial dislocation remained at the TB [38]. The TB provided more sites for dislocation nucleation and slip during the tension process, thus coordinating the plastic strain and improving the total elongation. In general, coherent TBs can not only effectively hinder the movement of dislocations, but also exert an effect similar to the strengthening of the traditional grain boundary. Moreover, the vicinity of TBs can provide sufficient space for dislocation storage, leading to the improvement of strength–ductility synergy.

4 Conclusions

(1) In traditional FSP, although decreasing the tool rotation rate can reduce the processing temperature from 462 to 402 °C, no change in the cooling rate of 16 °C/s occurred. By contrast, in CMA-FSP, the SZ showed a significantly decreased processing temperature (355 °C) and an increased cooling rate (47 °C/s) was obtained owing to the adoption of a liquid CO_2 coolant.

(2) The SZ in traditional FSP exhibited a fine grain structure with few substructures, and the grain size decreased with a reduction in the tool rotation rate. Owing to a decrease in the processing temperature and an increase in the cooling rate, the substructures produced during FSP could be retained in the grain, and grain coarsening was limited. Therefore, the SZ in CMA-FSP showed a fine grain structure with abundant dislocations and $\{10\bar{1}2\}$ twins. The grain refinement mechanism of the AZ31B Mg alloy during FSP was attributed to continuous DRX, discontinuous DRX, and twinning-induced geometric DRX.

(3) Strength and ductility were simultaneously improved because of the fine grain structure and randomized basal texture. Particularly in CMA-FSP, the SZ showed a best combination of ultimate tensile strength (293 MPa) and fracture elongation (18.6%). The $\{10\bar{1}2\}$ twins can provide adequate space for dislocation storage, making the plastic deformation more stable during tensile testing.

Acknowledgments

This work was supported by the Natural Science Foundation of Jiangsu Province, China (No. BK20211067), the National Natural Science Foundation of China (No. 51805145), and the Qing-Lan Project of Jiangsu Province, China.

References

[1] FAN Bo, ZHAO Long-sheng, FENG Zong-yu, LIU De-peng, YIN Wei-qiang, LONG Zhi-qi, HUANG Xiao-wei. Leaching behaviors of calcium and magnesium in ion-adsorption rare earth tailings with magnesium sulfate [J]. Transactions of Nonferrous Metals Society of China, 2021, 31: 288−296.

[2] KUMAR S D, KUMAR S S. Effect of heat treatment conditions on ballistic behaviour of various zones of friction stir welded magnesium alloy joints [J]. Transactions of Nonferrous Metals Society of China, 2021, 31: 156−166.

[3] LI Zi-han, ZHOU Guo-wei, LI Da-yong, WANG Hua-miao, TANG Wei-qin, PENG Ying-hong, ZUROB H S, WU Pei-dong. Crystal plasticity based modeling of grain boundary sliding in magnesium alloy AZ31B sheet [J]. Transactions of Nonferrous Metals Society of China, 2021, 31: 138−155.

[4] ZHAO Hong-liang, HUA Yun-xiao, DONG Xiang-lei, XING Hui, LU Yan-li. Influence of trace Ca addition on texture and stretch formability of AM50 magnesium alloy sheet [J]. Transactions of Nonferrous Metals Society of China, 2020, 30: 647−656.

[5] AHMADI S, ALIMIRZALOO V, FARAJI G, DONIAVI A. Properties inhomogeneity of AM60 magnesium alloy processed by cyclic extrusion compression angular pressing followed by extrusion [J]. Transactions of Nonferrous Metals Society of China, 2021, 31: 655−665.

[6] GAO Ming, ETIM I P, YANG Ke, TAN Li-li, MA Zheng. Enhancing mechanical property and corrosion resistance of Mg−Zn−Nd alloy wire by a combination of SPD techniques, extrusion and hot drawing [J]. Materials Science and Engineering A, 2022, 829: 142058.

[7] WANG Jun, YANG Xu-yue, LI Yi, XIAO Zhen-yu, ZHANG Du-xin, SAKAI T. Enhanced ductility and reduced asymmetry of Mg−2Al−1Zn alloy plate processed by torsion and annealing [J]. Transactions of Nonferrous Metals Society of China, 2015, 25: 3928−3935.

[8] PADHY G K, WU C S, GAO S. Friction stir based welding and processing technologies—Processes, parameters, micro-structures and applications: A review [J]. Journal of

Materials Science & Technology, 2018, 34: 1−38.

[9] MD F K, KARTHIK G M, PANIGRAHI S K, JANAKI RAM G D. Friction stir processing of QE22 magnesium alloy to achieve ultrafine-grained microstructure with enhanced room temperature ductility and texture weakening [J]. Materials Characterization, 2019, 147: 365−378.

[10] SONG Bo, YANG Qing-shan, ZHOU Tao, CHAI Lin-jiang, GUO Ning, LIU Ting-ting, GUO Sheng-feng, XIN Ren-long. Texture control by $\{10\bar{1}2\}$ twinning to improve the formability of Mg alloys: A review [J]. Journal of Materials Science & Technology, 2019, 35(10): 2269−2282.

[11] XIN Ren-long, LIU De-jia, XU Ze-ren, LI Bo, LIU Qing. Changes in texture and microstructure of friction stir welded Mg alloy during post-rolling and their effects on mechanical properties [J]. Materials Science and Engineering A, 2013, 582: 178−187.

[12] XU Nan, UEJI R, FUJII H. Enhanced mechanical properties of 70/30 brass joint by rapid cooling friction stir welding [J]. Materials Science and Engineering A, 2014, 610: 132−138.

[13] XU Nan, CHEN Lei, GU Bo-kun, REN Zi-ke, SONG Qi-ning, BAO Ye-feng. Heterogeneous structure-induced strength and ductility synergy of α-brass subjected to rapid cooling friction stir welding [J]. Transactions of Nonferrous Metals Society of China, 2021, 31: 3785−3799.

[14] ZHANG Hua, BAI Xiao-qing, HOU Min-jian, WANG Li-fei, ZHANG Qiang, FAN Jan-feng, WU Yu-cheng, DONG Hong-biao, XU Bing-she. Enhancing compressive mechanical properties of rolled AZ31 Mg alloy plates by pre-compression [J]. Materials Science and Engineering A, 2020, 772: 138686.

[15] LIU Fen-jun, JI Yan, SUN Zhi-yong, LIU Jian-bo, BAI Yan-xia, SHEN Zhi-kang. Enhancing corrosion resistance and mechanical properties of AZ31 magnesium alloy by friction stir processing with the same speed ratio [J]. Journal of Alloys and Compounds, 2020, 829: 154452.

[16] XU Nan, SONG Qi-ning, BAO Ye-feng. $\{10\bar{1}2\}$ twinning assisted microstructure and mechanical properties modification of high-force fiction stir processed AZ31B Mg alloy [J]. Materials Science and Engineering A, 2019, 745: 400−403.

[17] ZHOU Meng-ran, MORISADA Y, FUJII H. Effect of Ca addition on the microstructure and the mechanical properties of asymmetric double-sided friction stir welded AZ61 magnesium alloy [J]. Journal of Magnesium and Alloys, 2020, 8: 91−102.

[18] XU Nan, FENG Ruo-nan, GUO Wen-feng, SONG Qi-ning, BAO Ye-feng. Effect of Zener–Hollomon parameter on microstructure and mechanical properties of copper subjected to friction stir welding [J]. Acta Metallurgica Sinica (English Letters), 2020, 33: 319−326.

[19] CHANG C I, LEE C J, HUANG J C. Relationship between grain size and Zener–Holloman parameter during friction stir processing in AZ31 Mg alloys [J]. Scripta Materialia, 2004, 51: 509−514.

[20] KUMAR R, PANCHOLI V, BHARTI R P. Material flow visualization and determination of strain rate during friction stir welding [J]. Journal of Materials Processing Technology, 2018, 255: 470−476.

[21] SUH J, VICTORIA-HERNÁNDEZ J, LETZIG D, GOLLE R, VOLK W. Enhanced mechanical behavior and reduced mechanical anisotropy of AZ31 Mg alloy sheet processed by ECAP [J]. Materials Science and Engineering A, 2016, 650: 523−529.

[22] ZHAO Guang-wei, FAN Jian-feng, ZHANG Hua, ZHANG Qiang, YANG Jie, DONG Hong-biao, XU Bing-she. Exceptional mechanical properties of ultra-fine grain AZ31 alloy by the combined processing of ECAP, rolling and EPT [J]. Materials Science and Engineering A, 2018, 731: 54−60.

[23] ZHANG Hui, YAN Qi-qi, LI Luo-xing. Microstructures and tensile properties of AZ31 magnesium alloy by continuous extrusion forming process [J]. Materials Science and Engineering A, 2008, 486: 295−299.

[24] MIAO Qing, HU Lian-xi, WANG Guo-jun, WANG Er-de. Fabrication of excellent mechanical properties AZ31 magnesium alloy sheets by conventional rolling and subsequent annealing [J]. Materials Science and Engineering A, 2011, 528: 6694−6701.

[25] CHEN Juan, FUJII H, SUN Yu-feng, MORISADA Y, UEJI R. Fine grained Mg−3Al−1Zn alloy with randomized texture in the double-sided friction stir welded joints [J]. Materials Science and Engineering A, 2013, 580: 83−91.

[26] PARK S H, HONG S G, LEE C S. Activation mode dependent $\{10\bar{1}2\}$ twinning characteristics in a poly-crystalline magnesium alloy [J]. Scripta Materialia, 2010, 62: 202−205.

[27] XU Nan, ZHANG Wei-da, CAI Si-qi, ZHUO Yue, SONG Qi-ning, BAO Ye-feng. Microstructure and tensile properties of rapid-cooling friction-stir-welded AZ31B Mg alloy along thickness direction [J]. Transactions of Nonferrous Metals Society of China, 2020, 30: 3254−3262.

[28] XU Nan, FENG Ruo-nan, SONG Qi-ning, ZHAO Jian-hua, BAO Ye-feng. Influence of heterogeneous microstructures on the mechanical properties of low-temperature friction stir processed AZ91D Mg alloy [J]. Materials Science and Engineering A, 2021, 809: 141004.

[29] SUHUDDIN U F H R, MIRONOV S, SATO Y S, KOKAWA H, LEE C W. Grain structure evolution during friction-stir welding of AZ31 magnesium alloy [J]. Acta Materialia, 2009, 57: 5406−5418.

[30] HUMPHREYS F J, HATHERLY M. Recrystallization and related annealing phenomena [M]. 2nd ed. Amsterdam: Elsevier, 2004.

[31] LI Yuan, HOU Pei-jun, WU Zheng-gang, FENG Zhi-li, REN Yang, CHOO H. Dynamic recrystallization of a wrought magnesium alloy: Grain size and texture maps and their application for mechanical behavior predictions [J]. Materials & Design, 2021, 202: 109562.

[32] SAKAI T, BELYAKOV A, KAIBYSHEV R, MIURA H, JONAS J J. Dynamic and post-dynamic recrystallization under hot, cold and severe plastic deformation conditions [J]. Progress in Materials Science, 2014, 60: 130−207.

[33] FATEMI S M, PAUL H. Characterization of continuous dynamic recrystallization in WE43 magnesium alloy [J]. Materials Chemistry and Physics, 2021, 257: 123726.

[34] LIU Fen-jun, JI Yan, BAI Yan-xia. Influence of multipass high rotating speed friction stir processing on microstructure evolution, corrosion behavior and mechanical properties of stirred zone on AZ31 alloy [J]. Transactions of Nonferrous

Metals Society of China, 2020, 30(12): 3263−3273.
[35] AFRIN N, CHEN D L, CAO X, JAHAZI M. Strain hardening behavior of a friction stir welded magnesium alloy [J]. Scripta Materialia, 2007, 57: 1004−1007.
[36] SU Hu-hu, ZHOU Xin-zhe, ZHENG Shi-jian, YE Heng-qiang, YANG Zhi-qing. Atomic-resolution studies on reactions between basal dislocations and $\{10\bar{1}2\}$ coherent twin boundaries in a Mg alloy [J]. Journal of Materials Science & Technology, 2021, 66: 28−35.
[37] XIN Yun-chang, LV Liang-chen, CHEN Hou-wen, HE Cong, YU Hui-hui, LIU Qing. Effect of dislocation-twin boundary interaction on deformation by twin boundary migration [J]. Materials Science and Engineering A, 2016, 662: 95−99.
[38] WANG Fu-lin, AGNEW S R. Dislocation transmutation by tension twinning in magnesium alloy AZ31 [J]. International Journal of Plasticity, 2016, 81: 63−86.

冷媒辅助搅拌摩擦处理 AZ31B 镁合金的显微组织演变及力学性能

许 楠[1]，任紫科[1]，范 越[1]，顾帛坤[1]，沈 骏[2,3]，宋亓宁[1]，赵建华[1]，包晔峰[1]

1. 河海大学 机电工程学院，常州 213022；
2. 重庆大学 国家镁合金材料工程技术研究中心，重庆 400044；
3. 重庆大学 材料科学与工程学院，重庆 400044

摘 要：传统搅拌摩擦处理(FSP)后的 AZ31B 镁合金通常表现出强烈的基面织构，导致其强度和塑性匹配较差。本文作者采用冷媒辅助搅拌摩擦处理对 AZ31B 镁合金进行加工，研究液态二氧化碳冷却剂对搅拌区热循环、显微组织和力学性能的影响。使用液态二氧化碳同步冷却法可显著降低搅拌区的峰值温度并提高冷却速度，搅拌区出现具有大量位错和 $\{10\bar{1}2\}$ 孪晶的细晶结构。在不连续动态再结晶、连续动态再结晶和孪晶诱导几何动态再结晶的综合作用下，搅拌区发生显著的晶粒细化。拉伸试验中由于位错和 $\{10\bar{1}2\}$ 孪晶产生的交互作用，搅拌区的极限抗拉强度和断后伸长率分别达 293 MPa 和 18.6%，表现出良好的强度和塑性匹配。

关键词：镁合金；搅拌摩擦处理；Zenner−Hollomon 参数；再结晶；显微组织演变；力学性能

(Edited by Wei-ping CHEN)